





Radiation for laser-driven rescattering near the ultimate high-energy cutoff: The single-atom response and bremsstrahlung limit

Evan Jones , Zach Germain, Jakob Niessner, David Milliken, Joey Scilla, Liam Kelley , James MacDonald ,
and Barry C. Walker ^{*}

Department of Physics and Astronomy, University of Delaware, Newark, Delaware 19716, USA



(Received 29 October 2020; accepted 10 February 2021; published 22 February 2021)

The discovery of laser-driven rescattering and high harmonic radiation out to a maximum photon energy of 3.17 times the ponderomotive energy laid the groundwork for attosecond pulse generation and coherent x rays. As the laser field drives the interaction to higher energies, relativity and the Lorentz force from the laser magnetic field enter into the dynamics. Recent studies of laser rescattering have included these effects to give a quantitative description of rescattering dynamics in the high-energy limit, i.e., recollision energies of order 1,000 hartree (27 keV). In this high-energy limit, we treat the emitted high harmonic radiation from rescattering as a bremsstrahlung process. We find the highest-energy photons in the radiated energy spectra follow the rescattering electron energy near the ultimate cutoff. The effective charge from the ion core shielding does not affect the radiation yield at cutoff; however, the overall energy radiated does scale quadratically with the atomic number of the parent ion.

DOI: [10.1103/PhysRevA.103.023113](https://doi.org/10.1103/PhysRevA.103.023113)

I. INTRODUCTION

Strong-field, laser-driven rescattering [1] and the discovery of high harmonic radiation (HHG) [2] led to a revolution in laser science. The scientific push to generate spatially and temporally coherent x rays using HHG is an international quest now spanning three decades. This effort has achieved numerous milestones including the creation of sub-100-attosecond (atto = 10^{-18}) duration pulses [3–5] of soft-x-ray light.

Two critical aspects of marching into the frontiers of laser-driven acceleration are the laser characteristics and the high-energy recollision physics including relativistic effects [6–8]. The optimization of the laser-driven recollision is a complex physics parameter space that includes atomic, optical, and plasma physics. By way of example, this space has been searched out with studies of the laser carrier wavelength [9,10], laser intensity, phase matching and plasma dynamics [11], pulse duration, field ellipticity [12,13], and counterpropagating interference [14].

From the earliest studies of rescattering in strong laser fields, a classical physics description [15,16] was an essential part of understanding the new observations of HHG and multielectron excitation. Complicated multielectron dynamics [17,18] can be interpreted as classical electrons in a Coulomb potential interacting with a classical external laser electric field [19,20]. As the energy of the recollision process increases and the de Broglie wavelength of the electron decreases, the validity of the classical representation should only improve. With the complications of three-dimensional (3D) relativistic dynamics and multiply charged ion states, the

framework of classical physics is more essential to extend the initial insights into strong-field physics to higher intensities involving relativistic effects [21].

As the rescattering electron energy increases, it is deflected away from the parent ion by the Lorentz force from the laser magnetic field. A Lorentz deflection parameter [22,23] describes the degree of deflection and is given for an electron charge e and mass m_0 by

$$\Gamma_R = \frac{\sqrt{2I_P m_0 c^2 a_0^3}}{16\hbar\omega}, \quad (1)$$

where $a_0 = eE_0/(m_0 c \omega)$, c is the speed of light, I_P is the ionization potential energy, and E_0 and ω are the laser electric field magnitude and angular frequency, respectively. $\Gamma_R = 1$ serves as the demarcation between nonrelativistic and relativistic regimes [22].

Recollision near the HHG limiting cutoff [23] from relativistic deflection can be considered in a high-energy limit when compared to the atomic energy scale. That is, the photoelectron kinetic energy at the recollision (E_r) with the parent ion greatly exceeds the ionization energy for the atom of ion species under consideration. In this limit the atomic radiative recombination and dielectric recombination cross sections are known to scale as $\sim 1/(E_r)^2$ (see, e.g., Refs. [24–26]). Conversely, we find bremsstrahlung in this energy limit scales linearly with E_r . The energy increase for the recollision process results in bremsstrahlung [27,28] becoming an important mechanism. As an example, our calculations with $E_r = 1000$ hartree (27 keV) and a Ne^{2+} parent ion show the bremsstrahlung yield exceeds the recombination radiation into the ground state by two orders of magnitude.

We present here the limit for the HHG photon energy and yield from the fundamental single-atom radiation response

^{*}bcwalker@udel.edu

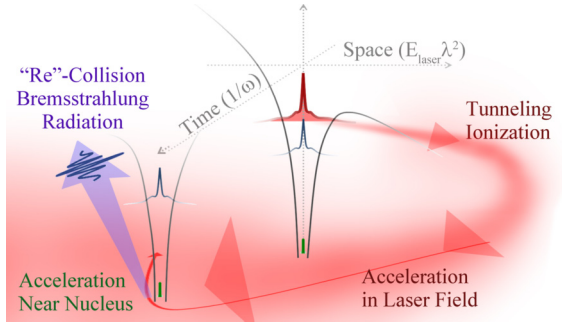


FIG. 1. Visual representation of tunneling ionization for the outermost electron, acceleration in the external laser field, and rescattering with the parent ion potential in the bremsstrahlung process.

with a few-cycle, linearly polarized drive laser. We find the expected radiation yield is primarily determined by the rescattering fluence, described relativistically and semiclassically, and the atomic number of the parent ion, which affects the bremsstrahlung mechanism. Radiation from rescattering has an ultimate energy cutoff that follows the ~ 1000 hartree energy cutoff for the rescattering electron fluence. Depending on the drive laser frequency and intensity, the radiation yield from rescattering can be significant across all atoms and ions in the periodic table.

II. METHOD OF CALCULATION

A. Dynamics of laser-driven bremsstrahlung collisions

Laser-driven rescattering begins when the external field ionizes the bound-state electron from the Coulomb potential, typically by tunneling (Fig. 1). Once in the continuum, the external laser field dominates the photoelectron dynamics. The photoelectron is initially pulled by the laser field away from the nucleus. Then, when the laser field direction reverses, the electron is accelerated back toward the parent ion with an energy gained by the work done on the electron in the external field. “Recollision” occurs for electrons that return to “reinteract” with the parent ion.

Recollision as a process extends up to an ultimate limit for the acceleration and rescattering energy [22,23] of order 1000 hartree. Electrons at 1000 hartree have a de Broglie wavelength ($\lambda_{\text{de Broglie}} = h/p$) of 0.14 bohrs, where a classical approach [19] can be considered valid for many atomic and molecular interactions. Viewing recollision in the classical regime is also consistent with the large $\sim e|E_0|/(m_0\omega^2)$ excursion distance for the photoelectron as it is driven by the laser field. Inelastic rescattering with the parent ion can create (e, ne) [29–31] secondary electrons, or HHG radiation.

We model the radiation process as a bremsstrahlung mechanism with the recollision occurring as the returning electron is accelerated by the parent ion potential. All results here are in the single-atom response limit and use plane-wave radiation for the laser field. We consider both the bare nucleus, where the interaction is between the incoming electron and the full nuclear charge, and scattering from the ion core shielded nucleus in the approximation of a centrosymmetric representation for the bound electrons [32]. The scattering process is calculated using classical, numerical-relativistic,

and well-known relativistic quantum [33] treatments for bremsstrahlung. The calculation of this process is connected to laser-driven bremsstrahlung in the laser plasma [34] and related as a physical process to a broad range of laser-driven phenomena including optical supercontinua [35]. The results are also relevant to calculations of coherently driven bremsstrahlung processes [36]. Far-reaching impacts may include attosecond bremsstrahlung [37] and measurements of electron wave functions in laser-assisted bremsstrahlung [38].

B. Rescattering model

The rescattering flux is determined by employing a semiclassical model previously described in Refs. [22,39]. Briefly, tunneling ionization is calculated using the Amosov, Delone, and Krainov (ADK) [40] rate. The electron wave packet is relativistically propagated in the external laser field using semiclassical trajectory ensembles. Relativistic effects do not drastically impact the ionization process [41] for all but the highest intensities used in these studies [42]. Even in these cases, while the ionization rate may need to be adjusted to account for the Lorentz electron drift during ionization, the ultimate cutoff of the bremsstrahlung results presented, which are presented normalized to account for small differences in ionization rates, will not be strongly affected.

Electron trajectories that return to the parent ion are used to calculate the rescattering fluence, which is approximated as a plane wave. This is a valid approximation considering the transverse width of the rescattering electron is many times greater than impact parameters responsible for bremsstrahlung. All results are for a $\sim 10\%$ ionization probability per optical cycle to create the species being studied; the single-atom response is considered to be below saturation [43]. To standardize the comparisons between atoms, we use a normalized flux \tilde{F}_R , i.e., the flux divided by the single-cycle ionization probability. This approach follows the convention of Ref. [23] and avoids nonphysical results due to the events at negligibly low event rates or due to nonadiabatic ionization where saturation effects occur on a timescale of less than a single cycle.

Examples of the energy-resolved rescattering flux [dimensionally electrons/(energy area)], i.e., the amount of the photoelectron returning to the parent ion as a function of the energy at the rescattering event, are shown in Fig. 2 for ionization in uranium. Uranium is the highest atomic number (Z) species considered in our study. The rescattering fluxes \tilde{F}_R in Fig. 2 show the nonrelativistic rescattering interaction with the well-known $3.17U_p$ scaling of the cutoff for $\Gamma_R < 1$. As the energy increases, rescattering reaches the onset of the ultimate limit for the cutoff at a collision energy around ~ 1000 hartree, beyond which the process transitions to the relativistic regime ($\Gamma_R > 1$).

From the figure, one can see rescattering as a physical process is not limited to one- or two-electron strong-field processes at mid-IR fields [44], rather, it is an inherent part of ionization across ion charge states, a wide range of laser wavelengths and intensities. By way of example we show in Fig. 2(a) the ionization of the highly charged U^{+34} by deep ultraviolet radiation with a wavelength of 100 nm at an intensity $\sim 10^3$ times greater than one atomic unit of intensity,

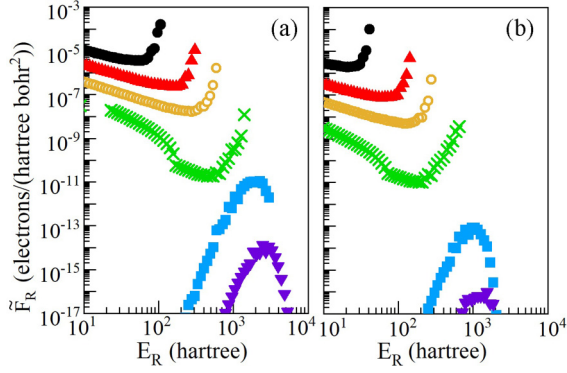


FIG. 2. Rescattering flux \tilde{F}_R as a function of the rescattering kinetic energy E_r for uranium ions driven by (a) 100-nm and (b) 800-nm lasers, respectively. The species shown for 100 nm are U^{20+} (black, circle) at $\Gamma_R = 0.06$ and 9.4×10^{17} W/cm², U^{25+} (red, triangle) at $\Gamma_R = 0.4$ and 2.7×10^{18} W/cm², U^{28+} (orange, open circle) at $\Gamma_R = 1$ and 5.4×10^{18} W/cm², U^{34+} (green, cross) at $\Gamma_R = 6$ and 1.3×10^{19} W/cm², U^{37+} (blue, square) at $\Gamma_R = 17$ and 2.7×10^{19} W/cm², and U^{44+} (purple, inverted triangle) at $\Gamma_R = 80$ and 6.7×10^{19} W/cm². The species shown for 800 nm are U^{7+} (black, circle) at $\Gamma_R = 0.06$ and 6×10^{15} W/cm², U^{10+} (red, triangle) at $\Gamma_R = 0.4$ and 2×10^{15} W/cm², U^{12+} (orange, open circle) at $\Gamma_R = 1$ and 4×10^{16} W/cm², U^{14+} (green, cross) at $\Gamma_R = 5$ and 9×10^{16} W/cm², U^{16+} (blue, square) at $\Gamma_R = 40$ and 3×10^{17} W/cm², and U^{20+} (purple, inverted triangle) at $\Gamma_R = 200$ and 8×10^{17} W/cm².

where the rescattering fluence is still significant and extends to ~ 1000 hartree as it enters into a relativistic interaction with $\Gamma_R = 6$.

Given the significance of relativity at the ultimate cutoff, it is prudent to consider relativistic effects for bremsstrahlung. We model the impact of relativity by modeling the recollision between a classical electron and a nuclear Coulomb potential, charge Z . We numerically solve the equations of motion with and without relativistic dynamics. Trajectories for 1000-hartree electron collisions with an argon nucleus at various impact parameters are shown in Fig. 3. These example trajectories in argon give an idea of the core penetration. The HHG process is fundamentally an atomic and molecular process. Relative to this perspective, Fig. 3 shows highly deflected trajectories, which experience the highest acceleration, are those with a closest approach to the atomic nucleus within the principle quantum number $n = 1$ bohr orbit. Impact parameters closer to the valence electron states are only slightly deflected. Just as the radius of curvature for the bound states scales as n^2 ,

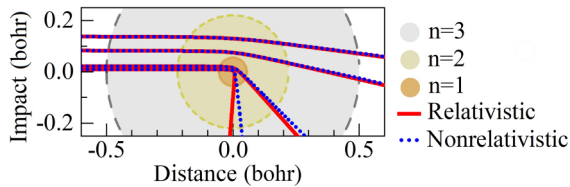


FIG. 3. Comparison of classical nonrelativistic (blue, dotted) and relativistic (red, solid) trajectories for 1000 hartree incident electrons upon a bare $Z = 18$ (argon) nucleus.

the deflection of the accelerated rescattering electron falls off quickly as one moves away from the nucleus.

For these 1000-hartree collisions, relativistic dynamics change the trajectory only for impact parameters, $b < 0.05$ bohrs, well inside the $n = 1$ electron state for argon and much smaller than $\lambda_{\text{de Broglie}}$ for an electron with a kinetic energy of 1000 hartree. The relativistic Lorentz factor for a 1000-hartree electron is $\gamma = 1.05$. It is therefore expected that, to a high degree of accuracy, the radiation process near the cutoff can be treated nonrelativistically.

C. Radiation calculations

We present the general formulation of calculating rescattering bremsstrahlung yields (hartree/hartree dimension for a single atom or ion) as a function of photon energy by

$$E_{\text{brem}}(E_\gamma) = \int \tilde{F}_R(E_r) \frac{d\chi(E_r, E_\gamma)}{dE_\gamma} dE_r, \quad (2)$$

where $\tilde{F}_R(E_r)$ is a generalized rescattering flux [electron/(energy area) dimension] as a function of the rescattering energy E_r , and $\chi(E_r, E_\gamma)$ is a generalized energy cross section [(energy area)/electron dimension] as a function of E_r and photon energy E_γ . Integrating Eq. (2) over E_γ gives the radiated energy per photon interval.

The radiation yield is calculated using three cross-section formulations. For the purpose of quantifying the differences of the approximations with each cross section in the clearest way, we use a monoenergetic flux of 1000-hartree incident electrons, $F_M(E_r) = \delta(E_r - 1000)$, where δ is the Dirac delta function. We chose $E_r = 1000$ hartree as the energy to show the rescattering physics for electron energies near the ultimate cutoff.

The first energy-resolved cross section is the classical, non-relativistic treatment [45] for bremsstrahlung,

$$\frac{d\chi_c}{dE_\gamma} = \frac{8}{3} \frac{e^6 Z^2}{\hbar m_e c^3} \frac{1}{E_r} \ln \left[\frac{\hbar}{e^2 m_e^{1/2}} \frac{(2E_r)^{3/2}}{ZE_\gamma} \right], \quad (3)$$

where Z is the atomic number and E_γ is the energy of the emitted photon.

The second energy cross section utilizes a numerical approach. We calculate the radiation spectra as defined by Ref. [45]. This approach gives the frequency and solid angle-resolved emission for a given trajectory solved using the relativistic equations of motion for the collision. The bremsstrahlung I (energy/electron dimension) for a given trajectory $\mathbf{r}(t)$ is given by

$$\frac{d[2I]}{dE_\gamma d\Omega} = K \left| \int_{-\frac{10 \text{ bohrs}}{v_0}}^{\frac{10 \text{ bohrs}}{v_0}} \frac{\mathbf{n} \times [(\mathbf{n} - \beta) \times \dot{\beta}]}{(1 - \beta \cdot \mathbf{n})^2} e^{i\omega[t - \frac{\mathbf{n} \cdot \mathbf{r}(t)}{c}]} dt \right|^2, \quad (4)$$

where $K = e^2/(4\pi^2 \hbar c)$, $\omega = E_\gamma/\hbar$, \mathbf{n} is the unit vector oriented in the direction of the observation point from a fixed centrosymmetric point potential, t is the time when the field

began propagating (retarded time), $\mathbf{r}(t)$ is the position of the electron measured from a fixed centrosymmetric point potential, v_0 is the magnitude of the initial velocity, $\beta = \mathbf{v}/c$, and $\dot{\beta} = \dot{\mathbf{v}}/c$. The bounds of the integration are set to cover the span of the collision, typically ± 10 bohrs.

We then perform the integration over the impact parameters b ,

$$\frac{d[2]\chi_N}{dE_\gamma d\Omega} = \int_{b_{\min}}^{b_{\max}} \frac{d[2]I}{dE_\gamma d\Omega} (2\pi b) db, \quad (5)$$

$$\begin{aligned} d\sigma_{\text{brem}} = & \alpha Z^2 \left(\frac{e^2}{\mu} \right)^2 \frac{p}{p_r} \frac{dE_\gamma}{E_\gamma} \left\{ \frac{4}{3} - 2E_r E \frac{(pc)^2 + (p_r c)^2}{(pc)^2 (p_r c)^2} + \mu^2 \left(\frac{\epsilon_r E}{(p_r c)^3} + \frac{\epsilon E_r}{(pc)^3} - \frac{\epsilon \epsilon_r}{(pc)(p_r c)} \right) \right. \\ & + \left[\frac{8}{3} \frac{E_r E}{(p_r c)(pc)} + \frac{E_\gamma^2}{(p_r c)^3 (pc)^3} [E_r^2 E^2 + (p_r c)^2 (pc)^2] \right] L \\ & \left. + \frac{\mu^2 E_\gamma}{2(pc)(p_r c)} \left[\frac{E_r E + (p_r c)^2}{(p_r c)^3} \epsilon_r - \frac{E_r E + (pc)^2}{(pc)^3} \epsilon + \frac{2E_\gamma E_r E}{(pc)^2 (p_r c)^2} \right] L \right\}, \quad (6) \end{aligned}$$

where p_r and p are the electron momentum (E_r and E for the energy) before and after rescattering, respectively. The emitted photon energy from the scattering is E_γ where $E_\gamma = E_r - E$. Other factors include $\alpha = e^2/\hbar c$, $\mu = mc^2$, $\epsilon = 2 \ln \left(\frac{E+(pc)}{\mu} \right)$, $\epsilon_r = 2 \ln \left(\frac{E_r+(p_r c)}{\mu} \right)$, and $L = 2 \ln \left(\frac{E_r E + (p_r c)(pc) - \mu^2}{\mu E_\gamma} \right)$.

The Bethe-Heitler cross section is the result of making the first Born approximation; the scattered electron wave is small compared to the incident wave and the scattered electron wave function is a combination of a plane wave and an outgoing spherical wave. This approximation is valid if $\alpha Z \ll |\beta|$. Equation (6) in the form of an energy cross section is

$$\frac{d\chi_{\text{BH}}}{dE_\gamma} = E_\gamma \frac{d\sigma_{\text{brem}}}{dE_\gamma}, \quad (7)$$

which allows us to make our yield comparison between the energy cross sections in Fig. 4.

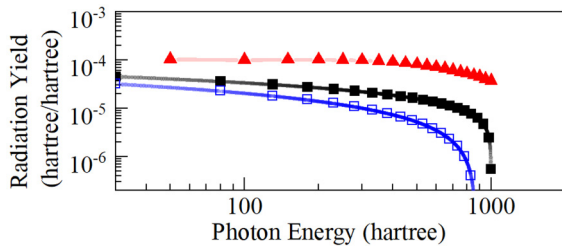


FIG. 4. Comparison of bremsstrahlung yields between classical nonrelativistic [blue, open square, Eq. (3)], solid angle integrated relativistic-numerical [red, triangle, Eq. (5)], and Bethe-Heitler [black, square, Eq. (7)] energy cross-section formulations. These yields are calculated [Eq. (2)] for a monoenergetic 1000-hartree electron flux, $F_M(E_r) = \delta(E_r - 1000)$, incident upon a bare nucleus uranium atom. For clarity, symbols in the figure are for a reduced number of points. Lines shown in the graph are a linear connection of the full calculated result.

which gives us our energy and solid angle-resolved relativistic-numerical energy cross section. The upper bound of the integration $b_{\max} = 100$ bohrs, while the lower bound b_{\min} is defined using the conventional method of the scattering electron de Broglie wavelength, $b_{\min} = \lambda_{\text{de Broglie}}$.

Finally, the third approach is the Bethe-Heitler cross section [33], $d\sigma_{\text{brem}}$ (area/electron dimension), which gives the relativistic, quantum bremsstrahlung emission from an unscreened Coulomb potential,

III. RESULTS AND DISCUSSION

A. Ion core screening

Multiple ionization in strong fields is predominantly a sequential process where the least tightly bound electrons are field ionized from the parent ion. With different laser field strengths and ionization states, recollision could occur with any residual charge for the parent ion core. Acceleration due to the effective charge of the scattering potential will vary from the parent ion residual charge to the full nuclear charge depending on the penetration of the impact parameter into the shielding ion core.

To compare the effect of electron shielding on radiation yields, we utilize numerical Dirac-Fock electron densities found in ELSEPA [32] to calculate the scattering potential with and without electron shielding. It is advantageous with this study of the HHG at the ultimate cutoff to show the impact of the ion core shielding using only the 1000-hartree F_M flux, which represents the portion of \tilde{F}_R near the ultimate cutoff.

We calculated the bremsstrahlung [using Eq. (5)] and F_M rescattering electrons with a fully shielded nucleus, i.e., scattering with a neutral parent ion, as well as a bare Z nucleus. The difference in the radiation yield for the fully shielded and bare nucleus with a lower Z species such as argon [Fig. 5(a)] is a factor of 2–3 depending on the scattering energy. The factor changes only slightly across the radiation frequency, which correlates with the impact parameter and penetration into the ion core; low-frequency scattering at high impact parameters sees the largest difference. For uranium the difference in the radiation yield is a factor of 6 across the frequency range plotted in Fig. 5(b). These are the two limiting cases for the scattering potentials from which the bremsstrahlung is generated; partially ionized species will have a radiation yield falling between these extremes. Given the predictable and minor factor of 2–6 scaling for radiation yields, we will exclude the ion core potential for all results shown in all subsequent figures.

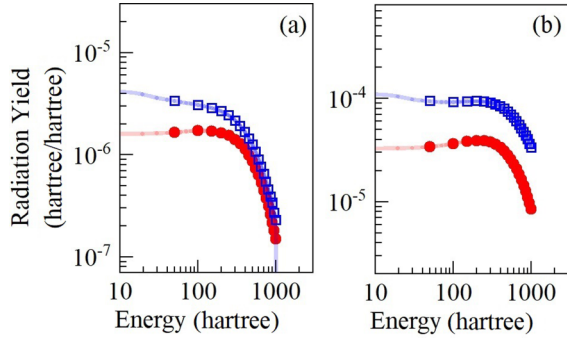


FIG. 5. (a) Argon and (b) uranium solid angle integrated relativistic-numerical yields [Eqs. (5) and (2)] calculated with a monoenergetic $F_M(E_r) = \delta(E_r - 1000)$ for a bare nucleus (blue, open square) and full electron shielding (red, circle). For clarity, symbols in the figure are for a reduced number of points. Lines shown in the graph are a linear connection of the full calculated result.

B. Atomic species dependence

The rescattering flux $\tilde{F}_R(E_r)$ and the energy cross section $\chi(E_r, E_\gamma)$ are independent functions in our method of calculation. Given this we can seek species with comparable \tilde{F}_R and different Z to determine the dependence of the radiation on the atomic species. Figure 6(a) gives \tilde{F}_R for three very different species that, however, all have a $\Gamma_R = 1$, the same 400-hartree rescattering cutoff energy, and similar ionization rates for the conditions given: Ne^{5+} and Kr^{8+} at 409 nm and 2.2×10^{17} W/cm², and U^{14+} at 304 nm and 3.9×10^{17} W/cm².

The Bethe-Heitler bremsstrahlung for these cases is shown in Fig. 6(b). Consistent with the common rescattering cutoff energy, the highest-energy radiation in all cases in Fig. 6(b) converges to 400 hartree. However, the overall HHG yields strongly depend on the atomic species with higher Z resulting in the greatest yield. Figure 6(b) includes superimposed yield lines with a Z^2 scaling. To a reasonable agreement, for nearly identical \tilde{F}_R the radiation yield near the ultimate cutoff can be expected to follow a simple Z^2 relationship. This understand-

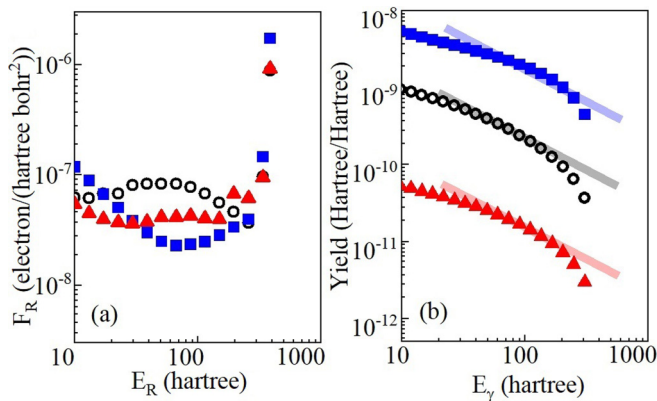


FIG. 6. (a) Numerical rescattering flux and (b) bremsstrahlung yields given by Eq. (2) with $\Gamma_R = 1$ for U^{14+} (square, blue) at 304 nm and 3.9×10^{17} W/cm², Kr^{8+} (open circle, black) at 409 nm and 2.2×10^{17} W/cm², and Ne^{5+} (triangle, red) at 409 nm and 2.2×10^{17} W/cm². Reference lines are projected onto (b) to indicate Z^2 scaled yields for U and Kr based on the relative yield from Ne.

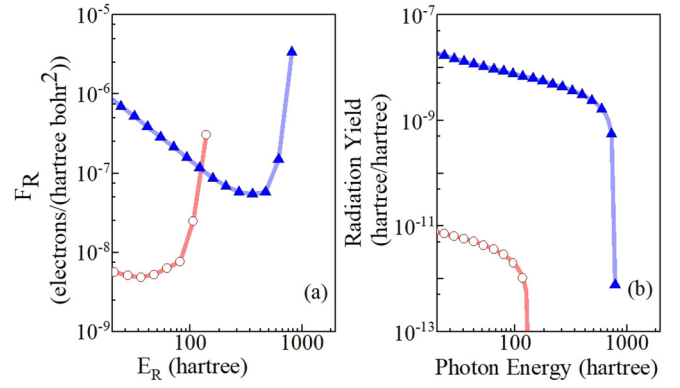


FIG. 7. Numerical rescattering flux and resulting bremsstrahlung yields [Eq. (2)] at $\Gamma_R = 1$ for U^{40+} (triangle, blue) at 5×10^{19} W/cm², $\lambda = 38$ nm, and Ne^+ (open circle, red) at 5×10^{14} W/cm², $\lambda = 5$ μm . For clarity, symbols in the figure are for a reduced number of points. Lines shown in the graph are a linear connection of the full calculated result.

ing of the radiation yield near the 1000-hartree cutoff allows an optimization of the radiation yield based on the atomic species.

HHG with neon is well understood in traditional strong fields with a $\Gamma_R = 1$ for the ionization of Ne to form Ne^+ at 5×10^{14} W/cm² with 5- μm light having an $\tilde{F}_R \sim 10^{-8}$ electrons/(hartree bohr²) and a cutoff near 100 hartree (3000 eV) in Fig. 7(a). The Bethe-Heitler yield from this rescattering gives an energy-resolved radiation of $\sim 10^{-11}$ hartree/(hartree) emitted per ionization event.

New x-ray free-electron lasers [46] and innovative XUV laser radiation sources [47] allow strong-field physics to explore new frontiers in HHG. Our calculations show for the ionization of U^{39} to form U^{40} with 38-nm light at 5×10^{19} W/cm², a $\Gamma_R = 1$ rescattering process can occur with \tilde{F}_R of order of $\sim 10^{-7}$ and radiation three orders of magnitude higher ($\sim 10^{-8}$ hartree/hartree in Fig. 7) than for neon in a strong field while having a cutoff approaching 1000 hartree. Traditional strong-field results for the single-atom response dipole radiated power using the single-active-electron quantum [48] or semiclassical results [15] compared favorably with the yield for neon shown in Fig. 7.

C. Angular emission

We discuss finally the angular emission radiation pattern for the generated bremsstrahlung. The physics can again be conveyed using F_M . For this example with argon, we limit the collision to only positive impact parameters shown in Fig. 3 with an initial velocity direction $\hat{v} = \hat{x} = \hat{E}_{\text{field}}$. The angle-resolved bremsstrahlung energy integrated for photon energies from 300 to 1000 hartree is mapped onto a unit sphere in Fig. 8 for electrons directed along the \hat{x} , E_{field} direction. For reference, the dipole radiation for this case would be peaked along the \hat{y} , \hat{B} , and \hat{z} , \hat{k} direction with no emission in the direction of travel, i.e., \hat{E}_{field} . In this case the electron for our calculations is accelerated in one direction, rather than oscillating as with impact parameters uniformly distributed on both sides of the parent ion, i.e., positive and negative

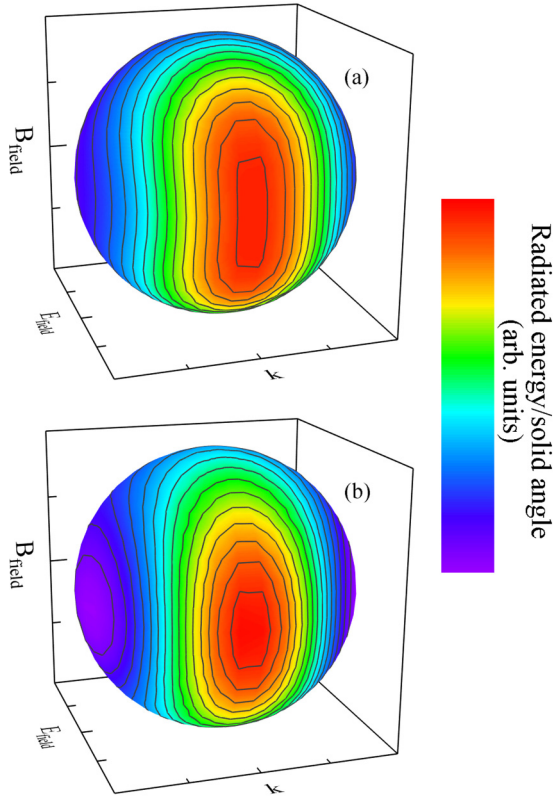


FIG. 8. (a) Angle-resolved total radiated energy cross section plotted on a unit sphere for photon energies between $E_\gamma = 300$ and 1000 hartree, and (b) total radiated energy from a 1000-hartree charged particle in 10° uniform circular motion from \hat{B} into \hat{E} . The bremsstrahlung yields are incident upon argon ($Z = 18$) at $E_R = 1000$ hartree. Note the radiation direction bias parallel to the incident particles' final momentum. The color scale is linear in the radiated energy from 0 (violet-blue) to the peak value (brightest red).

impacts for Fig. 3. As a result, only part of the azimuthal emission “doughnut” is observed. Full azimuthal symmetry would be observed for uniformly incident electrons (positive and negative b) also traveling in the \hat{x} and $-\hat{x}$ directions.

The limitation of impact parameters and direction chosen for Fig. 8 is helpful to see the physics of the collision near the cutoff. We can compare this complex laser-driven rescattering and radiation emission pattern in argon to that of a 1000-hartree electron traveling initially in the direction of \hat{x} , \hat{E}_{field} and undergoing a 10° arc of uniform circular motion. The angle-resolved bremsstrahlung emission for this second, pedagogical case is shown in Fig. 8(b). Note that the directions of the radiation for Figs. 8(a) and 8(b) are very close; HHG near the cutoff is similar to the radiation pattern from a small angle, i.e., of order $\sim 10^\circ$ arc, deflection of electrons with energies near the cutoff. The interaction of the rescattering electron with the parent ion is a complex process. However, using the comparison in Fig. 8 and the dependence of bremsstrahlung on acceleration, we can infer it is the closest approaching impact parameters that contribute strongly to the yield.

IV. CONCLUSION

We present the bremsstrahlung yields from laser-driven rescattering near the ultimate cutoff of HHG. Our findings show this regime can be accurately described as a semi-classical process where relativity must be included for the acceleration of the rescattering photoelectron but can be neglected when calculating the radiation from the collision. The shielding of the core electrons and ionization state of the parent ion affects the yield in a slight and predictable way, i.e., decreasing radiation from a fully shielded ion by a factor of a few compared to the unshielded nucleus. The radiation yield scales with the square of the nuclear charge Z^2 across atomic species. Optimization of the rescattering fluence near the cutoff by using short laser wavelengths and a high Z species such as uranium gives a radiation yield with a photon cutoff out to the region of the ultimate cutoff with a yield 10^3 higher than from neon with traditional strong-field, mid-IR light.

ACKNOWLEDGMENT

This material is based upon work supported by the National Science Foundation under Grant No. 1607321.

- [1] W. Becker, F. Grasbon, R. Kopold, D. Milosevic, G. Paulus, and H. Walther, in *Advances in Atomic Molecular and Optical Physics*, edited by B. Bederson and H. Walther, Vol. 48 (Academic, New York, 2002), pp. 35–98.
- [2] M. Ferray, A. L’Huillier, X. Li, L. Lompre, G. Mainfray, and C. Manus, *J. Phys. B* **21**, L31 (1988).
- [3] P. Paul, E. Toma, P. Breger, G. Mullot, F. Auge, P. Balcou, H. Muller, and P. Agostini, *Science* **292**, 1689 (2001).
- [4] Z. Chang and R. Y. Chiao, *Fundamentals of Attosecond Optics* (CRC Press, Boca Raton, FL, 2011).
- [5] T. Gaumnitz, A. Jain, Y. Pertot, M. Huppert, I. Jordan, F. Ardana-Lamas, and H. J. Worner, *Opt. Express* **25**, 27506 (2017).
- [6] N. Ekanayake, S. Luo, P. D. Grugan, W. B. Crosby, A. D. Camilo, C. V. McCowan, R. Scalzi, A. Tramontozzi, L. E. Howard, S. J. Wells, C. Mancuso, T. Stanev, M. F. Decamp, and B. C. Walker, *Phys. Rev. Lett.* **110**, 203003 (2013).
- [7] M. W. Walser, C. H. Keitel, A. Scrinzi, and T. Brabec, *Phys. Rev. Lett.* **85**, 5082 (2000).
- [8] M. C. Kohler, T. Pfeifer, K. Z. Hatsagortsyan, and C. H. Keitel, in *Advances in Atomic Molecular and Optical Physics*, edited by E. Arimondo, P. Berman, and C. Lin, Vol. 61 (Academic, New York, 2012), pp. 159–207.
- [9] D. Popmintchev, C. Hernandez-Garcia, F. Dollar, C. Mancuso, J. A. Perez-Hernandez, M.-C. Chen, A. Hankla, X. Gao, B. Shim, A. L. Gaeta, M. Tarazkar, D. A. Romanov, R. J. Levis, J. A. Gaffney, M. Foord, S. B. Libby, A. Jaron-Becker, A. Becker, L. Plaja, M. M. Murnane *et al.*, *Science* **350**, 1225 (2015).

- [10] Y. X. Zhang, S. Rykovanov, M. Shi, C. L. Zhong, X. T. He, B. Qiao, and M. Zepf, *Phys. Rev. Lett.* **124**, 114802 (2020).
- [11] T. Popmintchev, M.-C. Chen, D. Popmintchev, P. Arpin, S. Brown, S. Alisauskas, G. Andriukaitis, T. Balciunas, O. D. Muecke, A. Pugzlys, A. Baltuska, B. Shim, S. E. Schrauth, A. Gaeta, C. Hernandez-Garcia, L. Plaja, A. Becker, A. Jaron-Becker, M. M. Murnane, and H. C. Kapteyn, *Science* **336**, 1287 (2012).
- [12] O. Kfir, P. Grychtol, E. Turgut, R. Knut, D. Zusin, D. Popmintchev, T. Popmintchev, H. Nembach, J. M. Shaw, A. Fleischer, H. Kapteyn, M. Murnane, and O. Cohen, *Nat. Photonics* **9**, 99 (2015).
- [13] J. L. Chaloupka, *J. Phys. B* **53**, 185601 (2020).
- [14] J. Peatross, S. Voronov, and I. Prokopovich, *Opt. Express* **1**, 144 (1997).
- [15] P. B. Corkum, *Phys. Rev. Lett.* **71**, 1994 (1993).
- [16] K. Kulander, K. Schafer, and J. Krause, in *Super-Intense Laser-Atom Physics*, edited by B. Piraux, A. L'Huillier, and K. Rzazewski, NATO Advanced Studies Institute Series B: Physics (Plenum, New York, 1993), Vol. 316, pp. 95–110.
- [17] B. Walker, B. Sheehy, L. F. Dimauro, P. Agostini, K. J. Schafer, and K. C. Kulander, *Phys. Rev. Lett.* **73**, 1227 (1994).
- [18] R. Moshhammer, B. Feuerstein, W. Schmitt, A. Dorn, C. D. Schroter, J. Ullrich, H. Rottke, C. Trump, M. Wittmann, G. Korn, K. Hoffmann, and W. Sandner, *Phys. Rev. Lett.* **84**, 447 (2000).
- [19] P. J. Ho, R. Panfili, S. L. Haan, and J. H. Eberly, *Phys. Rev. Lett.* **94**, 093002 (2005).
- [20] W. Becker, X. Liu, P. J. Ho, and J. H. Eberly, *Rev. Mod. Phys.* **84**, 1011 (2012).
- [21] B. R. Galloway, D. Popmintchev, E. Pisanty, D. D. Hickstein, M. M. Murnane, H. C. Kapteyn, and T. Popmintchev, *Opt. Express* **24**, 21818 (2016).
- [22] S. Palaniyappan, I. Ghebregziabher, A. DiChiara, J. MacDonald, and B. C. Walker, *Phys. Rev. A* **74**, 033403 (2006).
- [23] M. Klaiber, K. Z. Hatsagortsyan, J. Wu, S. S. Luo, P. Grugan, and B. C. Walker, *Phys. Rev. Lett.* **118**, 093001 (2017).
- [24] H. Kramers, *Philos. Mag.* **46**, 836 (1923).
- [25] D. Verner, G. Ferland, K. Korista, and D. Yakovlev, *Astrophys. J.* **465**, 487 (1996).
- [26] S. N. Nahar and A. K. Pradhan, *Phys. Rev. A* **49**, 1816 (1994).
- [27] T. Hovhannisyan, A. Markossian, and G. Mkrtchian, *Eur. Phys. J. D* **20**, 17 (2002).
- [28] A. N. Zheltukhin, A. V. Flegel, M. V. Frolov, N. L. Manakov, and A. F. Starace, *J. Phys. B* **48**, 075202 (2015).
- [29] A. DiChiara, S. Palaniyappan, A. Falkowski, E. Huskins, and B. Walker, *J. Phys. B* **38**, L183 (2005).
- [30] A. D. DiChiara, E. Sistrunk, C. I. Blaga, U. B. Szafruga, P. Agostini, and L. F. DiMauro, *Phys. Rev. Lett.* **108**, 033002 (2012).
- [31] S. Palaniyappan, A. DiChiara, I. Ghebregziabher, E. L. Huskins, A. Falkowski, D. Pajerowski, and B. C. Walker, *J. Phys. B* **39**, S357 (2006).
- [32] F. Salvat, A. Jablonski, and C. J. Powell, *Comput. Phys. Commun.* **165**, 157 (2005).
- [33] H. Bethe and W. Heitler, *Proc. R. Soc. London, Ser. A* **146**, 0083 (1934).
- [34] S. Le Pape, L. Divol, A. Macphee, J. McNaney, M. Hohenberger, D. Froula, V. Glebov, O. L. Landen, C. Stoeckl, E. Dewald, S. Khan, C. Yeaman, P. Michel, M. Schneider, J. Knauer, J. Kilkenny, and A. J. Mackinnon, *High Energy Density Phys.* **31**, 13 (2019).
- [35] I. G. Koprnikov, A. Suda, M. Nurhuda, P. Wang, and K. Midorikawa, *Phys. Rev. A* **74**, 053819 (2006).
- [36] A. Balakin and G. Fraiman, *J. Exp. Theor. Phys.* **93**, 695 (2001).
- [37] G. Orlando, G. Castiglia, P. P. Corso, and E. Fiordilino, *J. Phys. B* **41**, 055601 (2008).
- [38] P. Corso, E. Fiordilino, and F. Persico, *J. Phys. B* **36**, 2823 (2003).
- [39] S. Palaniyappan, A. DiChiara, E. Chowdhury, A. Falkowski, G. Ongadi, E. L. Huskins, and B. C. Walker, *Phys. Rev. Lett.* **94**, 243003 (2005).
- [40] M. V. Ammosov, *Sov. Phys. JETP* **64**, 1191 (1987).
- [41] P. D. Grugan, S. Luo, M. Videtto, C. Mancuso, and B. C. Walker, *Phys. Rev. A* **85**, 053407 (2012).
- [42] C. J. Joachain and N. J. Kylstra, *Phys. Rev. A* **100**, 013417 (2019).
- [43] A. V. Bogatskaya, E. A. Volkova, V. Y. Kharin, and A. M. Popov, *Laser Phys. Lett.* **13**, 045301 (2016).
- [44] B. Wolter, M. G. Pullen, M. Baudisch, M. Sclafani, M. Hemmer, A. Senftleben, C. D. Schroter, J. Ullrich, R. Moshhammer, and J. Biegert, *Phys. Rev. X* **5**, 021034 (2015).
- [45] J. D. Jackson, *Classical Electrodynamics*, 3rd ed. (Wiley, New York, 1999), pp. 675 and 716.
- [46] N. Berrah, J. Bozek, J. T. Costello, S. Duesterer, L. Fang, J. Feldhaus, H. Fukuzawa, M. Hoener, Y. H. Jiang, P. Johnsson, E. T. Kennedy, M. Meyer, R. Moshhammer, P. Radcliffe, M. Richter, A. Rouzee, A. Rudenko, A. A. Sorokin, K. Tiedtke, K. Ueda *et al.*, *J. Mod. Opt.* **57**, 1015 (2010).
- [47] I. Makos, I. Orfanos, A. Nayak, J. Peschel, B. Major, I. Lontos, E. Skantzakis, N. Papadakis, C. Kalpouzos, M. Dumergue, S. Kuhn, K. Varju, P. Johnsson, A. L'Huillier, P. Tzallas, and D. Charalambidis, *Sci. Rep.* **10**, 3759 (2020).
- [48] J. L. Krause, K. J. Schafer, and K. C. Kulander, *Phys. Rev. Lett.* **68**, 3535 (1992).